DATA-DRIVEN SYSTEM IDENTIFICATION OF AN ACTIVE HELICOPTER ROTOR BLADE

S. Wisbacher*, J. Frey†, H. Pfifer†, D. Ossmann*

* Munich University of Applied Sciences HM, Department of Mechanical, Automotive & Aeronautical Engineering, 80335 Munich, Germany

† Technische Universität Dresden, Chair of Flight Mechanics and Control, 01307 Dresden, Germany

Abstract

Active control concepts for helicopter rotors, such as trailing edge morphing structures, offer significant potential for vibration reduction, noise mitigation, and performance improvement. An effective usage of these additional control inputs requires linear, control-oriented models that accurately capture the relevant rotor dynamics while remaining suitable for advanced model-based control design methods. This article presents a data-driven methodology to derive linear state-space representations from high-fidelity nonlinear rotor simulations, providing a systematic transition from detailed geometrical and aerodynamic modeling to control-oriented models. The proposed approach is based on subspace system identification and explicitly exploits the degrees of freedom provided by the algorithm to ensure both model fidelity and suitability for advanced control designs. The proposed methods are easily adaptable to real test data if flight measurements are available. The methodology is successfully demonstrated on a Bo 105 rotor blade simulator equipped with a trailing edge morphing structure.

Keywords

Data-driven System Identification; Control-oriented Modeling; Helicopter Rotor Active Control

1. INTRODUCTION

High vibration levels have long been identified as a primary factor affecting subsystem reliability, maintainability and life-cycle costs for helicopters [1]. A variety of effects factor into the high vibration levels, such as the interaction between a highly unsteady aerodynamic environment and rapidly rotating blades, high advancing blade Mach numbers and the effect of the rotor operating within its own wake [2]. While the helicopter development overall made great progress in performance, handling qualities, and efficiency, vibration and noise reduction remain a key factor to further improve helicopter development and thus continue to be a primary concern for the aircraft industry [3].

Given this sustained focus on vibration mitigation in rotorcraft research, numerous approaches for vibration reduction have been proposed over the past decades. A promising development is the integration of active control mechanisms on helicopter rotor blades, particularly in the form of active trailing edge morphing structures, which have been shown to enhance rotorcraft performance. Studies such as [4], [5] and [6] employ harmonic, open loop actuation of these morphing mechanisms to enhance rotor performance, achieving significant levels of vibration as well as power-consumption reductions. To fully exploit the potential of the morphing mechanisms and ensure performance improvements in the presence of disturbances, however, the development of modern robust control laws for actuating the additional control input is required. To enable the design of such control laws, the derivation of linearized rotor dynamics models including the morphing mechanism are essential.

There are different approaches found in literature to obtain linear models for helicopter rotors with the required characteristics. Analytical linear models are developed for rotors without active blades in [7], including flight-test based model validation. Analytical models for rotors equipped with trailing-edge flaps are derived in [8]. While analytical modeling offers a high degree of physical interpretability, it requires detailed and precise knowledge of all parameters influencing the blade dynamics and typically demands a substantial adaptation effort when applied to different rotor configurations. Data-driven approaches on the other side of the spectrum offer an alternative to this analytical modeling. In [9], a frequency-domain system identification method is used to identify a linear model of a UH 60 rotor with individual blade pitch based on flight-test data. A black-box subspace identification is applied in [10] to derive a linear model for an A109c rotor without active blades in hover condition, demonstrating the validity of such data-driven approaches for deriving linear models.

doi: 10.25967/650034

In this article, a subspace black-box identification approach, described in Section 2, is adopted to derive linear rotor models for a Bo 105 rotor augmented with an active trailing-edge morphing structure from non-linear simulation data. The non-linear simulator of the augmented blade, described in detail in Section 3, is implemented using the software ASWING, which enables the provision of detailed aerodynamic, structural, and control-response analysis of flexible aircraft structures [11]. The gathered simulation data as substitute of real flight test data is used to identify a linear model of the rotor dynamics in response to specifically designed actuations of the morphing structure in hover, as outlined in Section 4. The resulting model is validated in Section 5 using a different set of excitation signals in simulation scenarios independent of the identification process, finally confirming the approach's applicability to realistic operating conditions.

2. SYSTEM IDENTIFICATION FUNDAMENTALS

System identification is a core element of system theory that focuses on developing mathematical models to provide insight into system dynamics [12]. The resulting models support applications such as experiment designs, prediction of system behavior and controller design, which often rely on the availability of linear models. There are various types of model structures that can be used as mathematical representations for the system dynamics ranging from *white box* models based on physical laws with corresponding parameters and *gray box* models with adjustable parameters to subspace based *black box* models [12]. The choice between those option for a given problem generally depends on factors like prior knowledge of the system dynamics, available equipment to obtain data and requirements of the model. While *white box* and *grey box* modeling approaches rely heavily on prior knowledge and assumptions about the system dynamics to construct linear models, *black box* identification provides a way of deriving linear models without requiring prior specifications. Linear model representations suitable for control design are obtained directly from gathered input-output data. In this work a *black box* subspace identification algorithm is employed to derive a linear model of the helicopter rotor dynamics in response to deflections of the trailing edge morphing camber.

Different subspace identification methods are available in literature, e.g., canonical variate analysis, N4Sid, or the Multivariable Output-Error-State-Space (MOESP) algorithm, see, e.g. [13] for a comprehensive overview. In this work the MOESP algorithm is used, since it provides a numerically efficient and robust way to identify a linear model from simulation data. The fundamentals of the MOESP algorithm following [14] on which the approach herein is based is presented in what follows.

Subspace based modeling methods generally provide a discrete linear time invariant model given in its state space form as

$$\begin{aligned} x(k+1) &= Ax(k) + Bu(k) \\ y(k) &= Cx(k) + Du(k), \end{aligned} \tag{1}$$

with the system matrices $A \in \mathcal{R}^{n\times n}$, $B \in \mathcal{R}^{n\times p}$, $C \in \mathcal{R}^{q\times n}$ and $D \in \mathcal{R}^{q\times p}$. The vectors $x(k) \in \mathcal{R}^{n}$, $u(k) \in \mathcal{R}^{p}$ and $y(k) \in \mathcal{R}^{q}$ denote the states, inputs and outputs of the system, respectively, at a discrete time instance k. The challenge for subspace identification algorithms is to correctly assign the coefficients to the system matrices, given that no structure is previously defined and the output signal contains both the system's inherit dynamics as well as the dynamics enforced by the input. To be able to separate the components, the input/output data from the experiment is rearranged to form signal spaces that are linked by the model's system matrices in the so called data equation. To form the data equation the state space representation in Eq. (1) is first reformulated to the input-output model

$$y(i) = C\left(A^i x(0) + \sum_{k=0}^{i-1} A^{i-k-1} B u(k)\right) + Du(i) \tag{2}$$

that relates every instance i of the system response back to its initial state condition $x(0)$, the system matrices and the time history of the input signal u. For one sequence of an input/output data-set starting at the time instance i and of length s, this can be written as

$$\begin{bmatrix} y(i) \\ y(i+1) \\ y(i+2) \\ \vdots \\ y(s) \end{bmatrix} = \mathcal{O}_s x(i) + \mathcal{T}_s \begin{bmatrix} u(i) \\ u(i+1) \\ u(i+2) \\ \vdots \\ u(s) \end{bmatrix}. \tag{3}$$

with the extended observability matrix

$$\mathcal{O}_s = \begin{bmatrix} C & CA & CA^2 & \vdots & CA^{s-1} \end{bmatrix}^\top \tag{4}$$

and the matrix

$$\mathcal{T}_s = \begin{bmatrix} D & 0 & 0 & \dots & 0 \\ CB & D & 0 & \dots & 0 \\ CAB & CB & D & & 0 \\ \vdots & & \ddots & \ddots & \\ CA^{s-2}B & CA^{s-3}B & \dots & CB & D \end{bmatrix}. \tag{5}$$

As the system dynamics are considered to be time-invariant, the equation can be adapted for many sequences without changing $\mathcal{O}_s$ and $\mathcal{T}_s$. The output data is then structured as

(6)
$$Y_{i,s,N} = \begin{bmatrix} y(i) & y(i+1) & \dots & y(i+N) \\ y(i+1) & y(i+2) & \dots & y(i+N+1) \\ \vdots & \vdots & \ddots & \vdots \\ y(i+s) & y(i+1+s) & \dots & y(i+N+s) \end{bmatrix},$$

where N is the number of sequences that can be obtained from the data set. The input data is structured similarly and the initial state is adapted as

(7)
$$X_{i,N} = \begin{bmatrix} x(i) & x(i+1) & \dots & x(i+N) \end{bmatrix}.$$

The signal spaces together with the extended observability matrix $\mathcal{O}_s$ and the matrix $\mathcal{T}_s$ then form the data equation

(8)
$$Y_{i,s,N} = \mathcal{O}_s X_{i,N} + \mathcal{T}_s U_{i,s,N}.$$

For the implementation of the algorithm the length s of the sequences is generally referred to as the subspace dimension. There are restraints for choosing the subspace dimension, i.e., it has to be higher than the number of states of the identified model. The sequence length however also influences the number of sequences that can be obtained from one data set and thus defines both dimensions of the signal spaces. If sequences are too long it can sometimes lead to problems with detecting slower dynamics.
From the data equation in Eq. (8) the system's inherent dynamics can be isolated by using the nullspace $\Pi^{\perp}_{U_{0,s,N}}$ of the input signal space. With the nullspace the influence of the input on the output is removed and Eq. (8) reduces to

(9)
$$Y_{i,s,N}\Pi^{\perp}_{U_{i,s,N}} = \mathcal{O}_s X_{i,N}\Pi^{\perp}_{U_{i,s,N}},$$

which relates the content of the output signal space $Y_{i,s,N}$ that is only dependent on the systems inherent behavior with the system's A and C matrices. Since the system is assumed to be linear the extended observability matrix and thus A and C can be calculated from the column space of the reduced output space $(Y_{i,s,N}\Pi^{\perp}_{U_{i,s,N}})$. This leads to A and C matrices with entries which while featuring no direct physical interpretation still represent the system dynamics. If the original data is perfectly linear, the rank of the reduced output space directly corresponds to the number of states required to represent the system's dynamics. For non-linear data, however, an appropriate number of states must be chosen manually and used as a criterion for truncating the rank of the reduced output matrix.
With the A and C matrices known the B and D matrices from Eq. (1) can be found by solving Eq. (2) as a least square problem. In the non-linear case the quality and characteristics of the resulting model depend significantly on the subspace dimensions that define the shape of the reduced output space as well as the number of states used to truncate it. Thus, herein, these parameters will be used as explicit tuning parameters to improve the performance of the gathered linear models of the active rotor dynamics.

3. BO 105 ACTIVE ROTOR MODEL

The helicopter rotor structure herein is based on a Bo 105 rotor with a radius of $R = 4.91$ m and blades which interoperate a static NACA 23012 airfoil. Each blade of the rotor is assumed to feature an active structure section. The width w of this active structure covers 85 % of the overall blade radius as illustrated in Fig. 1. The active structure mechanism affects the aft 20 % of the airfoil along the cordlength, while the front 80 % remain equivalent to the baseline NACA 23012 airfoil. The morphing mechanism itself is based on the active structure system referred to as the Fish Bone Active Camber proposed in [15] as a compliant morphing structure applicable to a wide range of fixed and rotary wing applications. The concept has been tested in a wind tunnel campaign in [16] demonstrating its advantages over conventional flapped airfoils, including a broader range of angles of attack with high lift-to-drag ratios.

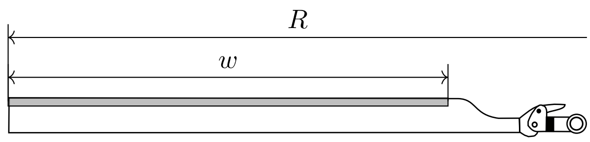

FIG 1. Geometric distribution of the active structure along the blade.

3.1. ASWING Simulation Setup

A nonlinear simulation model of the rotor with blades featuring active structures is set up in ASWING, a software for aerodynamic, structural, and control-response analysis of flexible aircraft [11]. The aerodynamics in ASWING are modeled via lifting-line theory with unsteady effects, explicitly taking the current circulation gradient into account. The trailing vortices align with the local inflow direction but are assumed to be straight, analogous to the assumption made for the circulation gradients. Aerodynamic characteristics of the airfoil are specified separately in a geometry model using support points along the structure. In between the support points the characteristic values are interpolated using splines. Compressibility is estimated via the Prandl-Glauert analogy.
A beam model is used to capture the elastic properties of the investigated rotor blade. Similar to the aerodynamic properties, all mechanical cross-sectional characteristics, with the exception of strength properties, are interpolated between specified support points. The aeroelastic simulation model is fully coupled, i.e., all forces external and inertial forces act on the deformed structure, as illustrated with the deflected blade in Fig. 2. This is especially

important for the modeling of the restoring effect of the centrifugal force on the blade.

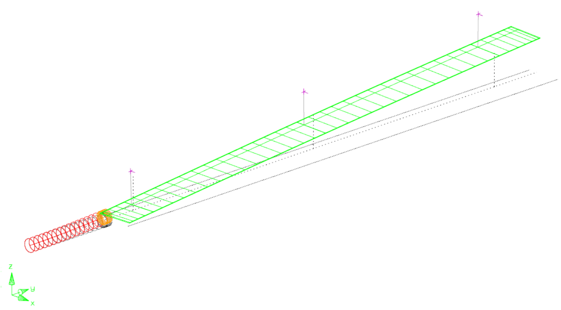

FIG 2. Bo 105 aeroelastic rotor blade model in ASWING.

The software ASWING generally allows for an almost arbitrary superposition of control surface deflections, whose effects are formulated through shifts in lift, profile drag, and pitching moment. The software enables spanwise distribution as well as the explicit specification of time histories for the control inputs, which is necessary for generating the system identification simulation scenarios. To capture the local flow quantities, accelerations, deformations, and internal forces resulting from a morphing deflection, virtual sensors can be placed in, on, and near the structure. For the rotor blade herein, three sensors are placed along the blade span and one additional sensor is placed at the blade root to capture quantities as blade root forces and moments. To further increase the realism of the simulation, a non-homogeneous flow field is modeled by superposing gust functions. This resembles the interaction between the rotor blades that usually occurs due to the rotor operating in its own wake. This setup ultimately enables a realistic representation of the blade dynamics of the full rotor while requiring the simulation of only a single active blade. This approach effectively reduces the computation time of the model without large negative effects on the accuracy.

3.2. Active Blade Model Implementation

The final blade model of the Bo 105 including the morphing mechanism consists of a beam segment at the blade root, representing the blade joint, and a wing segment in the airfoil-shaped region, with the geometric and mechanical parameters specified based on the available data in [17] and [18]. A structural damping, defined by the normal strain damping time ($t_{d\epsilon}$) and the shear strain damping time ($t_{d\gamma}$) according to the program's conventions is assumed with $t_{d\epsilon} = t_{d\gamma} = 0.1\,$s to stabilize the simulation. The aerodynamic characteristics of the baseline NACA23012 airfoil are obtained from the subsonic airfoil development system XFOIL [19], with a slight adjustment of the drag coefficient to account for the variation of Reynolds number over the blade radius. Blade pitch is implemented via an imaginary flap (F_1), which affects lift according to the airfoil lift-curve slope and has no effect on the pitch moment. The active structure is incorporated as a second flap (F_2), corresponding to the effect of a morphing mechanism as described in [20] with a hinge at the aforementioned $80\,\%$ of the cord length. A key aspect in this context is the ratio between the effects of the morphing mechanism on lift and its effect on the pitch moment. The lift and drag curves for the blade with the morphing structure are depicted in detail in Fig. 3. The deflection of the morphing mechanism leads to a parallel shift of the lift curves, while separation, i.e., stall, occurs earlier for positive deflections due to the increased camber. The pitching moment coefficient c_M is essentially shifted parallel when deflecting the mechanism. As depicted in the drag curves in the lower diagram of Fig. 3, the influence on the drag increases with an increasing lift coefficient, i.e., an increasing angle of attack. For angles of attack up to 5° both pressure and total drag is barely effected by the deflection of the morphing mechanism's flap.
The virtual sensors in the simulation model are placed at the blade root and provide loads at the clamped root over time. This mimics the installation location of real sensors in rotor tests and thus increases the realism of the proposed system identification. The model is set into motion by specifying a kinematic condition for the blade origin point, which simultaneously defines the origin of the model-fixed coordinate system. The imposed kinematics consist of velocity, yaw rate and radial acceleration. For the identification, a hover scenario is simulated, in which the origin point (R_{ref}) follows a circular trajectory. Finally, the imposed kinematics for the rotor in hover condition together with the main structural, geometric and aerodynamic parameters of the blade model are provided in the appendix in Table 2 and Table 3, respectively.

4. ROTOR BLADE SYSTEM IDENTIFICATION

The linear model to be identified needs to capture the dynamic relationship between the morphing input and the resulting structural loads. To obtain the required data for identification, a hover condition is simulated in which the operating trajectory of the blade remains constant over each rotor revolution (P). During the simulation, the pitch angle is kept fixed, whereas the morphing angle is excited using a chirp input as depicted in the upper diagram of Fig. 4. The lower diagram in Fig. 4 illustrates that this designed chirp signal covers frequencies from 1.5-$6\,P$. This range ensures adequate excitation of the blade dynamics within the relevant frequency band for, e.g., load control design. All three blade root forces F_x, F_y, F_z and blade root moments M_x, M_y, M_z in a blade fixed coordinate system are selected as output signals as they provide valuable insight in the blade motion. The blade fixed coordinate system is illustrated on the active rotor blade in Fig. 5. It is defined with the x-axis directing into the rotor plane pointing in the direction the blade moves, the y-axis also in the rotor plane pointing along the blade, and the z-axis pointing upwards out of the rotor plane. Since the coordinate system is blade fixed, it rotates with the current rotor speed.

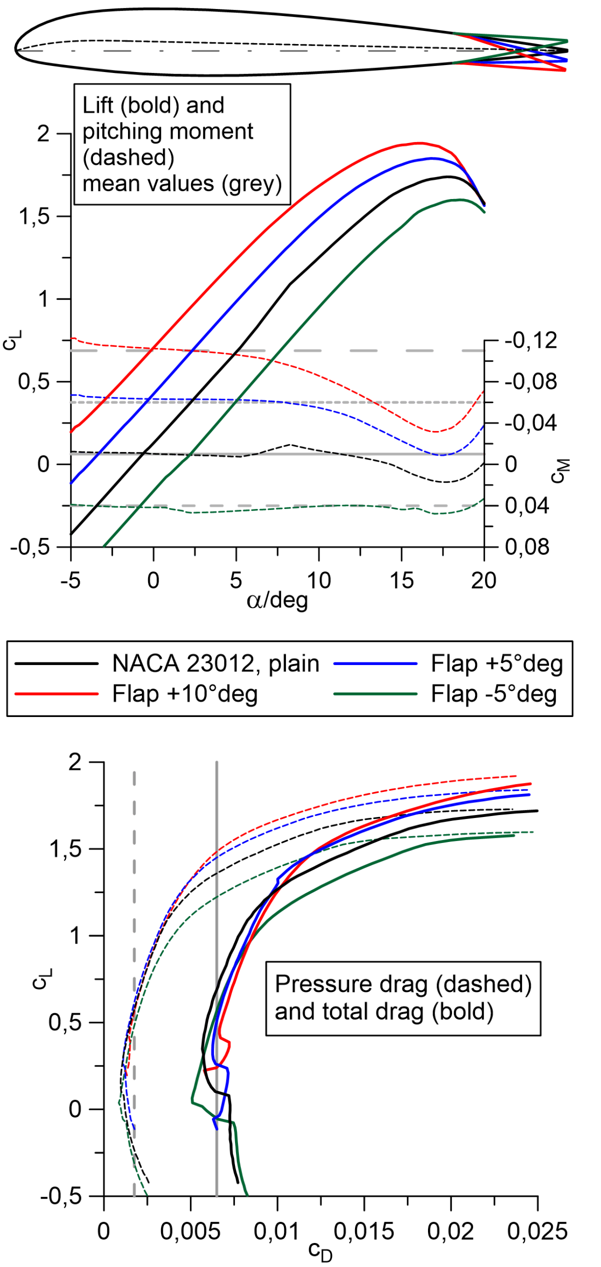

FIG 3. Lift and drag curves for the NACA 23012 airfoil with active structure at a Reynolds number of Re=$3 \cdot 10^6$.

4.1. Data Analysis

To ensure that the collected simulation results can be represented with a linear model, the data is analyzed using a coherence spectrum. The coherence spectrum κ_{uy} of an input signal u and an output signal y is calculated as

$$\kappa_{uy}(\omega) = \sqrt{\frac{\Phi_{uy}^2(\omega)}{\Phi_{uu}(\omega)\Phi_{yy}(\omega)}} \tag{10}$$

with the cross-correlation spectrum Φ_{uy} and the auto-correlations Φ_{uu} and Φ_{yy} of the two signals. The coherence value can vary between 0 and 1 with values close or equal to zero meaning that the two investigated signals are uncorrelated [21]. Values close or equal to one on the other hand indicate that the output signal is correlated with the input signal and can thus be predicted linearly from it.

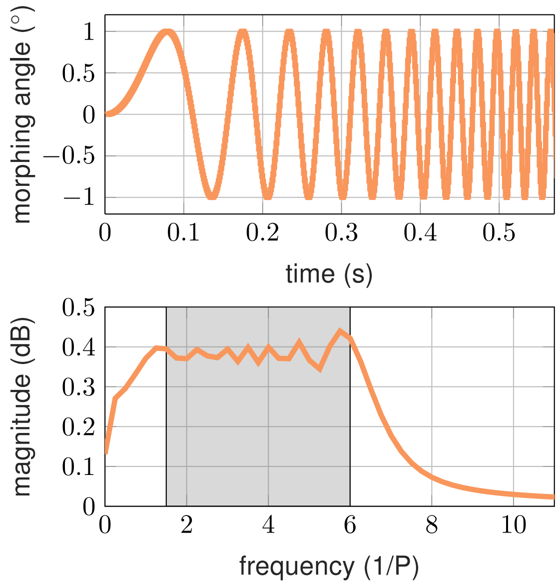

FIG 4. Identification input signal shape and spectrum.

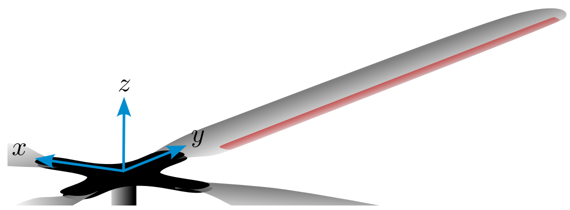

FIG 5. Rotor blade with the active structure and the defined blade-fixed coordinate system.

Figure 6 depicts the simulation results for the most dominant output channels F_z and M_x in the upper diagram and their respective coherence spectra below. The coherence is specifically high for frequency from 1.5-$8\,P$, indicating that a linear model can adequately represent the dynamics of the blades within the frequency range that was excited with the input signal. Note that the coherence spectra are similar across all six output channels.

4.2. Subspace Identification

As discussed in Section 2, the defined subspace dimension as well as the selected number of states for the linear model that are used within the identification algorithm have significant influence on the quality of the resulting model. To quantify this quality of the resulting models the actual fitness values are proposed herein. The fitness value

$$f_y = 100\left(1 - \frac{||y - \hat{y}||_2}{||y - \bar{y}||_2}\right), \tag{11}$$

expressed in percent, compares the predicted output $\hat{y}$ of the identified model with the measured data y. It represents a normalized prediction error, where the l_2 norm of the prediction error is normalized by the

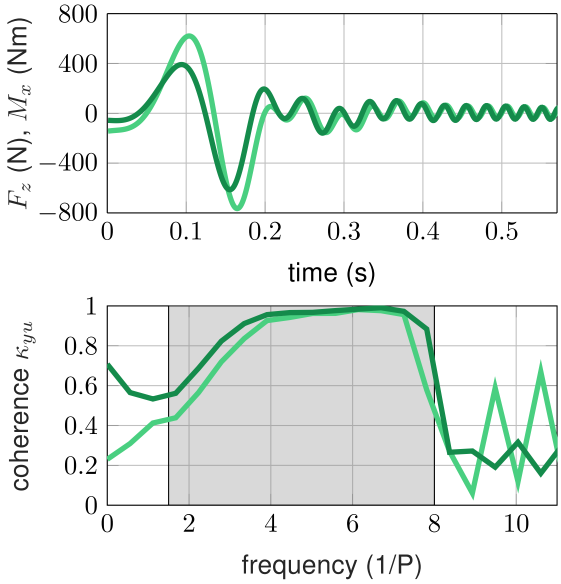

FIG 6. Time domain response and coherence spectra of the output channels F_z (—) and M_x (—) in response to the defined chirp signal.

l_2 norm of the data centered around its mean value $\bar{y}$. Since both norms are computed over the same dataset, this metric is equivalent to a normalized root mean square error (NRMSE). A fitness value of 0 % indicates that the NRMSE between the model output and the simulation data is equal to the NRMSE obtained by comparing the data to its mean value. The fitness value may become negative, which indicates that the model prediction error exceeds the variability of the data around its mean, for example due to a significant constant offset or poor dynamic agreement between the model response and the data.

The average fitness value over all six output channels of the rotor model is used to evaluate how well the dynamics of the resulting models using different subspace dimensions and number of states match the simulation reference. For each defined number of states, identification is performed using 30 different subspace dimensions. Note that the identification configurations have to be chosen such that the subspace dimension exceeds the number of states of the resulting system. The resulting average fitness values for state dimensions of 2 (∘), 4 (□) and 6 (△) are shown in Fig. 7. The results indicate that the best possible model has 6 states and is identified with 30 subspace dimensions providing an average fitness value of about 77.6 %. With respect to model-based control designs, however, it is desirable to identify low order models. A similarly good average fitness can be achieved with a fourth order model, identified using 29 subspace dimensions. With its average fitness of 77.2 % this selected fourth order model lies only 0.5 % below the fitness value of the sixth order model while featuring two states less.

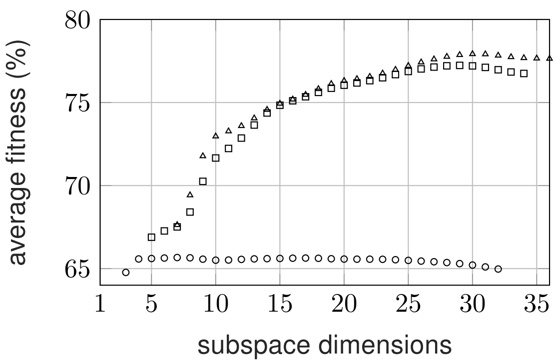

FIG 7. Average fitness values over subspace dimensions for identified models of state dimension 2 (∘), 4 (□) and 6 (△).

4.3. Identification Results

The performance of the resulting linear, fourth order model (—) from Section 4.2 against the available data (—) is depicted in Fig. 8 for the force responses and in Fig. 9 for the moment responses in all three axes. The most dominant output channels are F_z and M_x since these are most strongly influenced by the change in lift generated by the morphing deflections. The model captures these effects very well, achieving fitness values around 88 % to 90 %, respectively. Since the blade is slightly V-shaped and bends due to the distribution of the change of lift along the blade, the influence of the morphing deflection is also noticeable in F_y. For this channel again, the corresponding plot shows good agreement between model response and the original data, which is confirmed by a

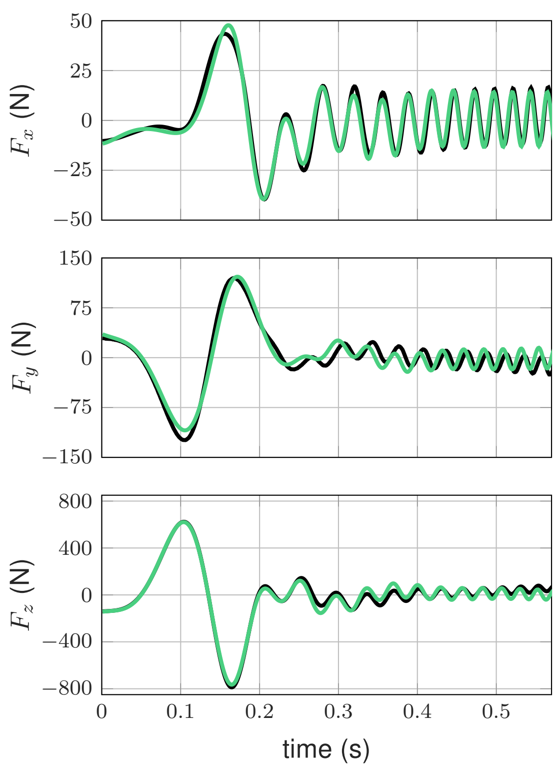

FIG 8. Nonlinear simulation (—) versus identified linear model force responses (—) for the identification scenario.

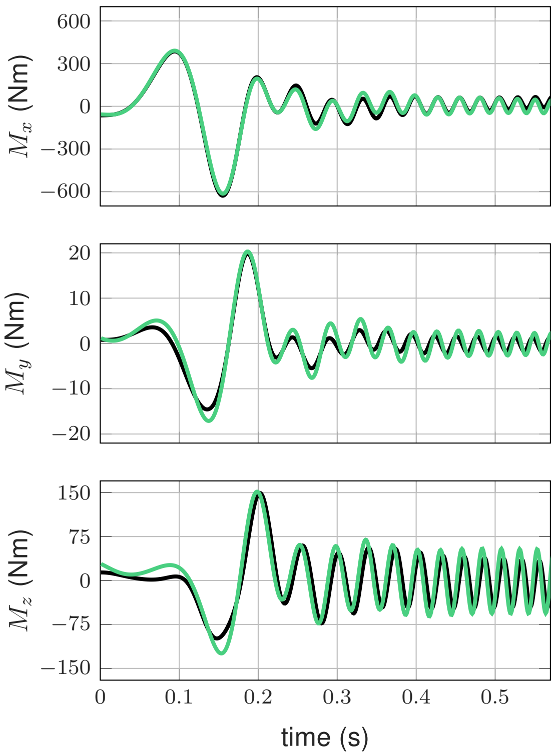

FIG 9. Nonlinear simulation (——) versus identified linear model moment responses (——) for the identification scenario.

fitness value of about $76\,\%$. The deflection of the morphing mechanism also creates a blade torsion M_y. This blade torsion, however, is small due the short lever-arm resulting from the changed neutral point. The identified model captures this effect with a fitness value of about $76\,\%$. The in-plane bending moment M_z of the blade proves to be the most difficult channel to identify. Since it is only indirectly excited by the relatively small change in drag force of the blade caused by the angle of attack change when deflecting the morphing mechanism, only a fitness value of around $52\,\%$ is reached. This is, however, still acceptable as this motion is not the main goal of control algorithms targeting load and noise reductions. Finally, the F_x channel attains a satisfactory fitness value of about $81\,\%$.

The poles of the identified model are shown in Fig. 10. The identified eigenfrequencies are located at approximately 14.9 rad/s and 46.3 rad/s, which corresponds to 0.3 /rev and 1.1 /rev, respectively. The higher-frequency mode exhibits a damping ratio of about 0.3, whereas the lower-frequency mode has a damping ratio of approximately 0.55. Overall, with one eigenfrequency located at approximately half the rotor frequency and another close to the rotor frequency, the identified eigenmodes are within a plausible range for a Bo 105 rotor blade.

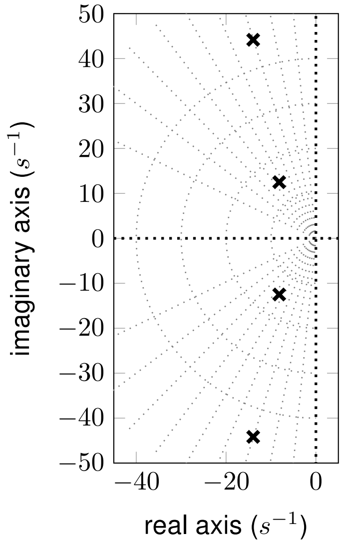

FIG 10. Pole positions of the identified system.

5. LINEAR MODEL VALIDATION

The identified linear model is validated using simulation runs that are independent from the identification process to ensure that the model dynamics accurately represent the original behavior across all output channels. Specifically, another chirp (——) input and an impulse (——) input, both depicted in the upper diagram of Fig. 11, are applied. The chirp input differs from the identification chirp input in both amplitude and frequency range. Its frequency spectrum, depicted in the lower diagram of Fig. 11, lies predominantly in a lower range than that of the identification signal. The frequency spectrum of the impulse signal (——), also depicted in the lower diagram of Fig. 11, is mostly constant across all frequencies, but shows a lower magnitudes within that range compared to the chirp. This makes it a challenging excitation signal

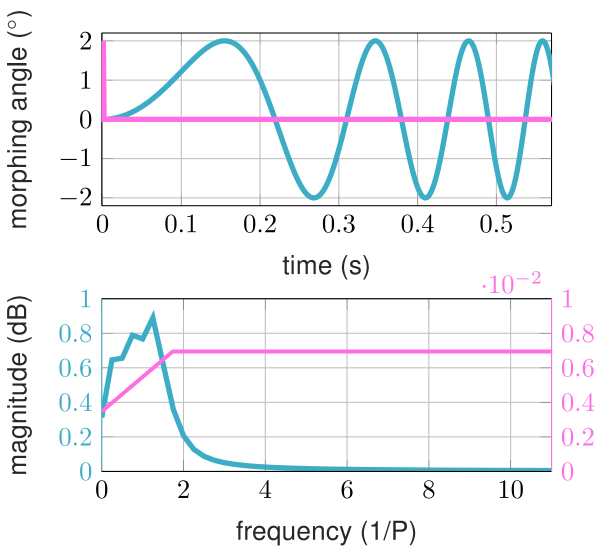

FIG 11. Chirp (——) and impulse (——) input signals and spectra for validation.

that is used to validate how well the linear system captures small and fast dynamics.

The resulting model responses for the chirp (—) and impulse (—) are depicted together with the nonlinear simulation results (—) in Fig. 12. Again, for both input scenarios the main response is within the F_z and M_x channels. For the chirp, the linear model responses achieve a fitness in those two signals of about $86\,\%$ similar to the identification case. For the impulse, the fitness is slightly lower with values of $71\,\%$ to $74\,\%$. This is due to the impulse having a constant excitation spectrum also at higher frequencies. These frequencies are not fully captured by the model due to the input design spectrum for the identification process described in Section 4.1. Overall the fitness values for those two main output channels are still satisfactory and indicate that the linear model captures the active blade behavior. For the F_y and M_y channels the fitness values of the model compared to the identification are successfully maintained for the chirp input at around $81\,\%$ for F_y, and $82\,\%$ for M_y , respectively. For the impulse $38\,\%$ are achieved for F_y and $67\,\%$ for M_y. The significantly lower fitness values for impulse compared to the chirp indicate that at low frequencies the dynamics in these two channels are captured adequately by the model. A substantial contribution is, however, present at higher frequencies, which is not captured well by the model if excited. Similarly, F_x and M_z are is still captured adequately at low frequencies with a fitness value of about $66\,\%$ to $78\,\%$ for the chirp input. For the impulse input the combination of low signal magnitude and model inaccuracies at high frequencies lead to a significantly reduced fitness of about $28\,\%$ for F_x, while the value for M_z even falls below zero.

The exact fitness values of the six individual output channels for both validation input scenarios together with the fitness values from the identification are outlined in Table 1. To summarize, the model captures the dynamics connected to the dominant output channels F_z and M_x very well. It struggles to capture the in-plane dynamics F_x and M_z, that are excited less by the blade morphing. For the F_y and M_y channels the accuracy decreases, however, only at higher frequency. These frequencies are out of scope of any morphing control algorithms. Thus, despite some deficiencies in certain channels and frequencies, the derived model enables advanced, model-based control designs for the morphing mechanism.

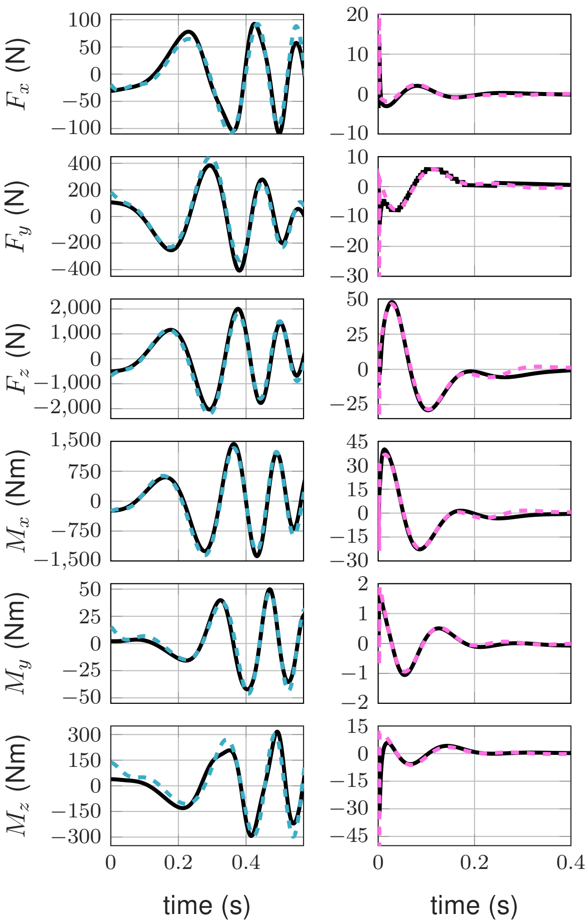

FIG 12. Validation of the identified linear model against the nonlinear simulation (—) for a chirp (—) and an impulse (—).

TAB 1. Validation fitness values in percent.

	F_x	F_y	F_z	M_x	M_y	M_z
identif.	81.1	76.4	88.2	89.6	75.9	52.3
chirp	78.5	80.8	85.4	86.5	81.7	66.3
impulse	27.9	38.4	71.3	73.6	67.7	<0

6. CONCLUSIONS

This paper presents a control-oriented, subspace-based system identification approach to capture the dynamics of a Bo 105 rotor equipped with a trailing-edge morphing structure in hover, with a particular focus on the response to morphing actuation. Blade root forces and moments obtained from a high-fidelity nonlinear simulation serve as identification data, which makes the proposed methodology readily transferable to experimental rotor test data. Within the identification procedure, the subspace algorithm parameters are systematically optimized to obtain a linear model that is controllable and accurately represents the relevant rotor dynamics. Validation shows that the model reliably reproduces the dominant dynamic behavior directly excited by the morphing input. These results indicate that the identified model is well suited for subsequent control design and analysis involving morphing-based rotor actuation.

Contact address:

sabine.wisabcher@hm.edu

References

[1] Angelo C. Veca. Vibration effects on helicopter reliability and maintainability. Tech-

nical report, Defense Technical Information Center, Fort Belvoir, VA, USA, 1973. DOI: 10.21236/AD0766307.

[2] S. R. Viswamurthy and R. Ganguli. Performance sensitivity of helicopter global and local optimal harmonic vibration controller. *Computers & Mathematics with Applications*, 56(10):2468–2480, 2008. DOI: 10.1016/j.camwa.2008.05.034.

[3] Ch. Kessler. Active rotor control for helicopters: Motivation and survey on higher harmonic control. *CEAS Aeronautical Journal*, 1:3–22, 2011. DOI: 10.1007/s13272-011-0005-9.

[4] Dominik Komp, Sumeet Kumar, Manfred Hajek, and Jürgen Rauleder. Effect of active camber morphing on rotor performance and control loads. *Aerospace Science and Technology*, 2021. DOI: 10.1016/j.ast.2020.106311.

[5] Sumeet Kumar, Dominik Komp, Manfred Hajek, and Juergen Rauleder. Effect of active camber on rotor noise, power and hub vibration. In *Proceedings of the AIAA SciTech Forum*, Virtual Event, 2021. DOI: 10.2514/6.2021-1927.

[6] Dominik Komp, Manfred Hajek, and Juergen Rauleder. Rotor performance enhancements with spanwise varying active camber morphing. In *Proceedings of the AIAA SciTech Forum*, Virtual Event, 2021. DOI: 10.2514/6.2021-0200.

[7] Patrick T. Jensen, H. C. Curtiss, and Robert M. McKillip. An analytically linearized helicopter model with improved modeling accuracy. NASA Contractor Report 188715, NASA Ames Research Center, 1991.

[8] T. A. Millott and P. P. Friedmann. Vibration reduction in helicopter rotors using an actively controlled partial-span trailing-edge flap located on the blade. NASA Contractor Report 4611, NASA Ames Research Center, 1994.

[9] Umberto Saetti, Joseph F. Horn, Tom Berger, Mark J. S. Lopez, and Mark B. Tischler. Identification of linear time-periodic systems from rotorcraft flight-test data. *Journal of Guidance, Control, and Dynamics*, 42(10):2288–2296, 2019. DOI: 10.2514/1.G004406.

[10] Sergio Bittanti and Marco Lovera. Identification of linear models for a hovering helicopter rotor. In *Proceedings of the IFAC Symposium on System Identification*, Fukuoka, Japan, 1997. DOI: 10.1016/S1474-6670(17)42840-0.

[11] Mark Drela. Integrated simulation model for preliminary aerodynamic, structural, and control-law design of aircraft. In *Proceedings of the 40th AIAA Structures, Structural Dynamics, and Materials Conference and Exhibit*, St. Louis, MO, USA, 1999. DOI: 10.2514/6.1999-1394.

[12] Karel J. Keesman. *System Identification: An Introduction*. Advanced Textbooks in Control and Signal Processing. Springer, London, UK, 2011. DOI: 10.1007/978-0-85729-522-4.

[13] S. Joe Qin. An overview of subspace identification. *Computers & Chemical Engineering*, 30(10–12), 2006. DOI: 10.1016/j.compchemeng.2006.05.045.

[14] Michel Verhaegen. Subspace techniques in system identification. In John Baillieul and Tariq Samad, editors, *Encyclopedia of Systems and Control*. Springer, London, UK, 2014. DOI: 10.1007/978-1-4471-5102-9_107-1.

[15] Benjamin King Woods and Michael I. Friswell. Preliminary investigation of a fishbone active camber concept. In *Proceedings of the ASME Conference on Smart Materials, Adaptive Structures and Intelligent Systems*, Stone Mountain, GA, USA, 2012. DOI: 10.1115/SMASIS2012-8058.

[16] Benjamin King Woods, Onur Bilgen, and Michael I. Friswell. Wind tunnel testing of the fish bone active camber morphing concept. *Journal of Intelligent Material Systems and Structures*, 25(7):772–785, 2014. DOI: 10.1177/1045389X14521700.

[17] Oliver Dieterich, Joachim Götz, Marilena Pavel, Binh DangVu, Pierangelo Masarati, Giuseppe Quaranta, Massimo Gennaretti, Jacopo Serafini, Michael Jump, and L. Liu. Rigid body and aeroelastic rotorcraft-pilot coupling (RPC) – prediction tools and means for prevention. Technical Publication 167, GARTEUR, 2008.

[18] James R. Van Gaasbeek. Validation of the rotorcraft flight simulation program (C81) using operational loads survey flight test data. Technical Report ADA089008, Defense Technical Information Center, Fort Belvoir, VA, USA, 1980.

[19] Mark Drela. XFOIL: An analysis and design system for low reynolds number airfoils. In *Low Reynolds Number Aerodynamics*, Notre Dame, IN, USA, 1989.

[20] Jürgen Rauleder, Berend G. van der Wall, Amine Abdelmoula, Dominik Komp, Sumeet Kumar, Vaclav Ondra, Branislav Titurus, and Benjamin King Sutton Woods. Aerodynamic performance of morphing blades and rotor systems. In *Proceedings of the 74th Annual American Helicopter Society International Forum and Technology Display*, Phoenix, AZ, USA, 2018.

[21] Lennart Ljung. *System Identification: Theory for the User*. Prentice Hall Information and System Sciences Series. Prentice Hall PTR, Upper Saddle River, NJ, USA, 2nd edition, 1999.

A. ROTOR DATA

This section of the Appendix provides detailed geometrical and airfoil data of the modeled rotor in ASWING.

TAB 2. Geometry data

Radius	$R = 4.91$ m, airfoil starting at $r = 0.75$ m
Chord length	$c = 0.27$ m, constant from $r = 1.1$ m
Twist	$\Delta\varepsilon = -6.2\,°$ from $r = 1.1$ m
Rotational speed	$\omega_z = 2500\,°$/s
Origin point	$R_{\text{ref}} = 0.229$ m
Circulation speed	$u_{\text{ref}} = 10$ m/s
Radial acceleration	$a_{y,\text{ref}} = 463.33$ m/s^2

TAB 3. Airfoil data (NACA 23012, Re = $3 \cdot 10^6$)

Zero-lift angle	$\alpha_0 = -1.25\,°$
Lift-curve slope	$\frac{dC_L}{dF_1} = 0.1097/°$
Zero-lift pressure drag	$C_{D,p} = 0.00175$
Zero-lift skin friction drag	$C_{D,f} = 0.00475$
Zero pitch moment	$C_{M,0} = -0.01$
Morphing effectiveness in lift	$\frac{dC_L}{dF_2} = 0.06/°$
Morphing effectiveness in pitch moment	$\frac{dC_M}{dF_2} = -0.01/°$
Maximum lift coefficient	$C_{L,\text{max}} = 1.55$